Journal of Science and Technology in Transportation Volume 1 Issue 2, 2020
ISSN: 2710-XXXX DOI: 10.XXXX/jstit.202009_1(1).0001

Harmonic Characteristics Analysis of AC-DC-AC Locomotive Grid Side Current

Yao He[1, *]

[1] Southwest Jiaotong University, Chengdu, Sichuan, China

[*] Corresponding Email, yh111@qq.com

Abstract

The harmonic current at the grid side of AC-DC-AC locomotives is mainly generated by rectifiers. All AC-DC-AC locomotives introduced in China adopt single-phase four quadrant converters as locomotive rectifiers. The locomotive simulation model is established and compared with the measured data to study the harmonic characteristics of AC-DC-AC locomotive. The results show that the distribution law of main harmonic times of harmonic current at locomotive grid side under different power is consistent. The harmonic current distribution characteristics of AC-DC-AC locomotive have remarkable correlation with the effective value of fundamental current, showing significant nonlinear attenuation change. That is, when the fundamental current is small, the total distortion rate of harmonic current is large and the content of single harmonic current is high. When the fundamental current increases, the total distortion rate of harmonic current and the content of single harmonic current are significantly reduced.

Keywords

Harmonic characteristics; Locomotive; Grid side current

1 Introduction

In the late 1970s, China began to develop AC drive electric locomotive. In the early 1990s, the trial production of AC4000 AC drive electric locomotive was successful. Later, tests were carried out on Zhongyuan Star, Pioneer, Zhonghua Star and other models, and achieved success. In recent years, through the introduction, digestion and absorption of foreign AC drive technology and independent R & D innovation, a series of AC drive electric locomotives [1-3] and EMUs with world-class level such as HXD1, HXD2, HXD3, CRH1, CRH2, CRH3 and CRH5 have been developed and successfully applied. These AC drive electric locomotives and EMUs would gradually become the main models of high-speed railway and heavy haul lines in China.

ISSN: 2710-XXXX DOI: 10.XXXX/jstit.202009_1(1).0001

The intermediate DC link of AC-DC-AC locomotive [4-6] is connected in parallel with large support capacitance and second harmonic resonance circuit. The output voltage of rectifier is approximately DC. The high-order harmonic generated by inverter is weakened by the intermediate circuit, and only part of it is fed back to the power grid. Therefore, the harmonic current at the grid side of AC-DC-AC locomotive is mainly generated by rectifier [7-9]. Although there are different models of AC, DC and AC locomotives [10-12] introduced into China, they all use single-phase four quadrant converter as locomotive rectifier. By analyzing the four quadrant converters of different locomotives, we could get the harmonic generation mechanism and harmonic distribution characteristics of the whole locomotive [13-15].

The single-phase four quadrant converter used in AC-DC-AC locomotive has the advantages of high power-factor, low harmonic content and two-way flow of energy. The four-quadrant converter of AC-DC-AC locomotive [16, 17] includes both two-level four quadrant converter and three-level four quadrant converter. For AC-DC-AC locomotive, the traction converter assembly at the grid side could be equivalent to the equivalent circuit shown in Figure 1. Where, u_N is the voltage at locomotive grid side, in is the current at locomotive grid side, k is the transformation ratio of traction transformer Tr, i_x is the input current at AC side of traction converter [18-20], and are the equivalent resistance and inductance of traction transformer, and u_{ab} is the output voltage of four quadrant converter.

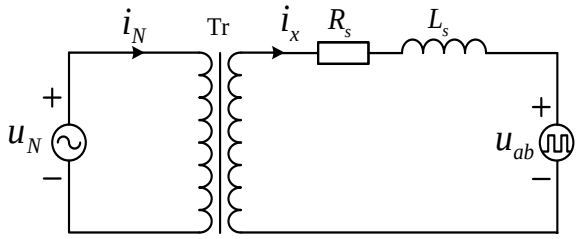

Figure 1 Equivalent circuit of traction converter for AC-DC-AC locomotive.

Because the internal resistance R_s of traction transformer is far less than its inductance L_s, its internal resistance can be ignored. Therefore, the above equivalent circuit could be further simplified, and the simplified equivalent circuit is shown in Figure 2, where L_N is the equivalent inductance at the grid side.

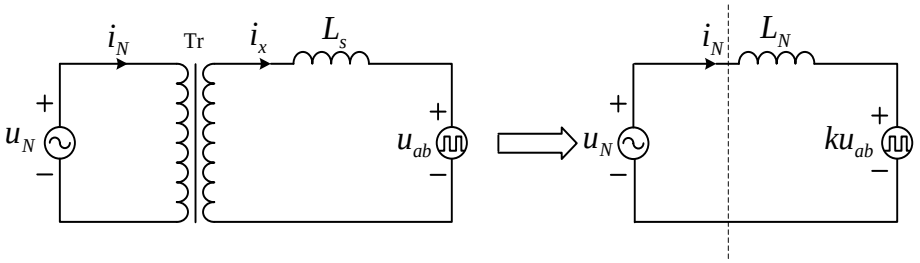

Figure 2 Simplified equivalent circuit of traction converter for AC-DC-AC locomotive.

ISSN: 2710-XXXX DOI: 10.XXXX/jstit.202009_1(1).0001

2 Mathematical analysis of harmonic current on AC-DC-AC locomotive grid side

Under traction condition, the phase difference between $\dot{I}_N$ and $\dot{U}_N$ is 0 degrees, and $\dot{U}_{ab}$ lags behind $\dot{U}_N$. For regenerative braking condition, the phase difference between $\dot{I}_N$ and $\dot{U}_N$ is 180 degrees. Under this condition, $\dot{U}_{ab}$ is ahead of $\dot{U}_N$, and the motor feeds back energy to the catenary through the traction converter. Under any working condition, the voltage vector balance equation of traction converter is always:

$$\dot{U}_N = j\omega L_N \dot{I}_N + \dot{U}_{ab}$$

According to the phasor diagram of traction converter at fundamental frequency, as shown in Figure 3, the fundamental wave component at grid side meets the following formula,

$$(\omega L_N I_N)^2 + U_N^2 = \left(\frac{kMU_d}{\sqrt{2}}\right)^2$$

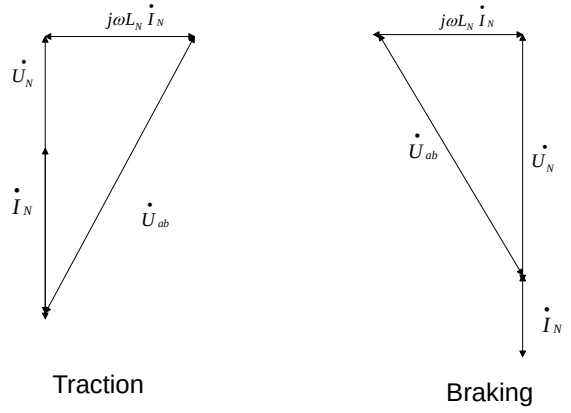

Figure 3 Phasor diagram of traction converter at fundamental frequency.

The fundamental component of the input current at the grid side is

$$I_N = \frac{kMU_d \sin\beta}{\sqrt{2}\omega L_N} = \frac{\sqrt{(kMU_d)^2/2 - U_N^2}}{\omega L_N}$$

Modulation ratio M and modulation wave phase angle β are respectively

$$\begin{cases} M = \dfrac{\sqrt{2}\sqrt{U_N^2 + (\omega L_N I_N)^2}}{kU_d} \\ \beta = \arctan\dfrac{\omega L_N I_N}{U_N} \end{cases}$$

For the harmonic component of grid side current, the grid side harmonic model is shown in Figure 4.

ISSN: 2710-XXXX DOI: 10.XXXX/jstit.202009_1(1).0001

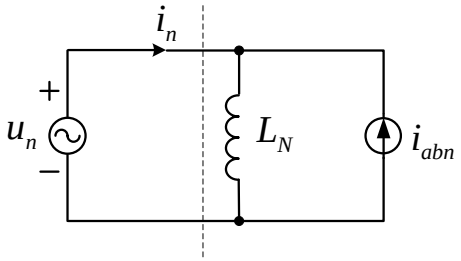

Figure 4 Harmonic equivalent model of converter grid side.

The harmonic current source is

$$i_{abn}=\frac{1}{L_N}\int ku_{abn}(t)dt=\sum_{m=2,4\cdots}^{\infty}\sum_{n=\pm1,\pm2\cdots}^{\infty}\left\{\begin{array}{l}\dfrac{2kU_{\mathrm{d}}J_n(mM\pi)}{m\pi L_{\mathrm{N}}(m\omega_{\mathrm{c}}+n\omega)}\sin\dfrac{n}{2}\pi\times\\ \sin(m\omega_{\mathrm{c}}t+n\omega t+n\beta+m\alpha)\end{array}\right\}$$

The expression of grid side input current is

$$i_N(t)=\pm\frac{\sqrt{(kMU_{\mathrm{d}})^2-2U_{\mathrm{N}}{}^2}}{\omega L_{\mathrm{N}}}\cos(\omega t)-\sum_{m=2,4\mathrm{L}}^{\infty}\sum_{n=\pm1,\pm2\mathrm{L}}^{\infty}\left\{\begin{array}{l}\dfrac{2kU_{\mathrm{d}}J_n(mM\pi)}{m\pi L_{\mathrm{N}}(m\omega_{\mathrm{c}}+n\omega)}\sin\dfrac{n}{2}\pi\times\\ \sin(m\omega_{\mathrm{c}}t+n\omega t+n\beta+m\alpha)\end{array}\right\}$$

Where "+" represents the input current of converter under traction condition and "-" represents the input current of converter under regenerative braking condition.

The harmonic component of the input current at the locomotive grid side is determined by the carrier wave and modulation wave. The current harmonic is mainly distributed near the even times of the carrier frequency, and the current harmonic frequency at the grid side is $(m\omega_{\mathrm{c}}/\omega_{\mathrm{m}}+n)$ pu. At the same time, the main harmonic distribution times of grid side current are independent of locomotive power and grid voltage, and are mainly related to carrier wave and modulation wave angular frequency. That is, the harmonic is $(m\omega_{\mathrm{c}}/\omega_{\mathrm{m}}+n)$, and its amplitude is related to regenerative braking power. Thirdly, under both traction and regenerative braking conditions, as long as the locomotive power and traction grid voltage remain constant, the distribution law of harmonic current at grid side remains consistent.

3 Harmonic characteristic analysis of AC-DC-AC locomotive

By changing the power of locomotive, the dynamic characteristics of harmonic current at locomotive grid side are simulated. Several different power points are selected and compared with the measured harmonic current spectrum of locomotive to study the distribution characteristics of harmonic current at locomotive grid side.

ISSN: 2710-XXXX DOI: 10.XXXX/jstit.202009_1(1).0001

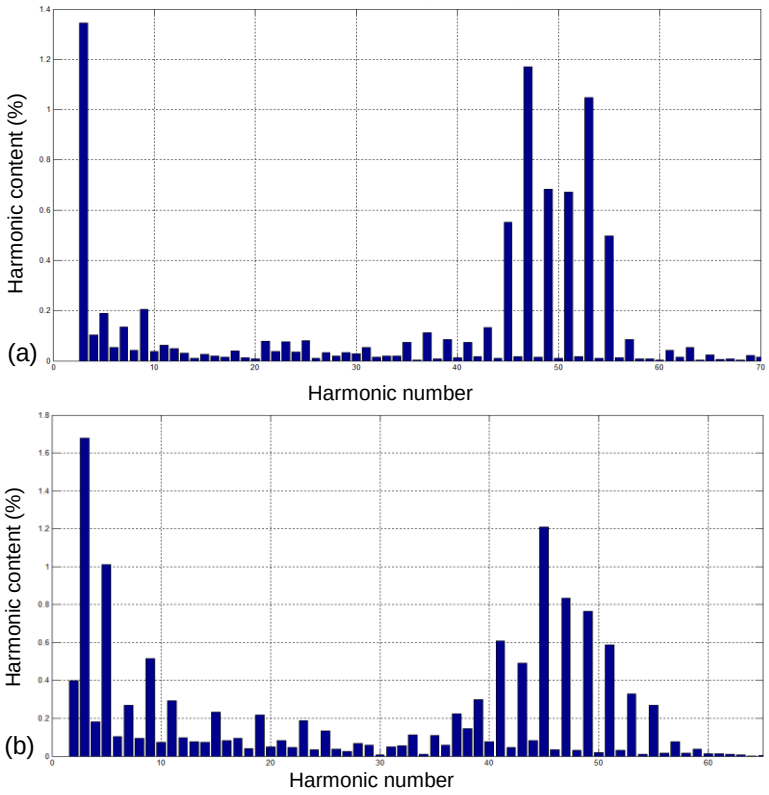

Figure 5 Harmonic current spectrum at grid side when *P*= 4800 kW, (a) simulation result, (b) measured result.

As can be seen from Figure 5, no matter the simulation results or the measured results, when the power is 2400kW, the harmonics of the grid side current are mainly 3, 5, 7, 9, 47, 49, 51 and 53, accounting for a large proportion. Comparing the simulation results with the measured results, it is found that the measured harmonic content of grid side current is larger than the simulation results.

ISSN: 2710-XXXX DOI: 10.XXXX/jstit.202009_1(1).0001

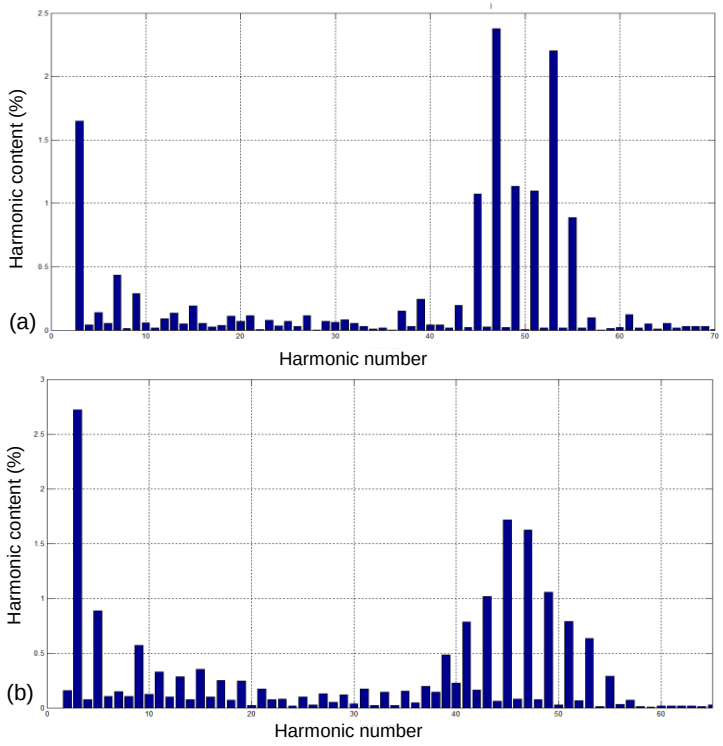

Figure 6 Harmonic current spectrum at grid side when *P*= 2400 kW, (a) simulation result, (b) measured result.

It can be found from Figure 6(a) that the 3rd, 47th and 53rd harmonic currents at the grid side are particularly significant, and the harmonic content is the largest. It can be seen from Figure 6 that the distribution law of the main harmonic times of the simulation results and the measured results is consistent.

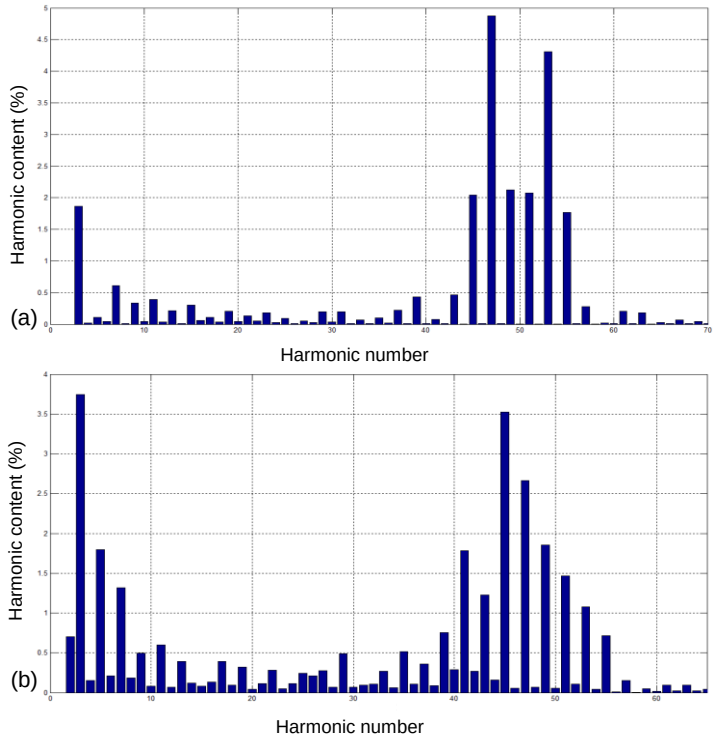

ISSN: 2710-XXXX DOI: 10.XXXX/jstit.202009_1(1).0001

Figure 7 Harmonic current spectrum at grid side when *P*= 1200 kW, (a) simulation result, (b) measured result.

In Figure 7(b), the low-order harmonics are mainly concentrated in the 3rd, 5th and 7th order, and the high-order harmonics are mainly concentrated in the 41st, 45th, 47th and 49th order. Figure 7 show that most of the harmonic contents of the test results are higher than the simulation results when *P*= 1200 kW.

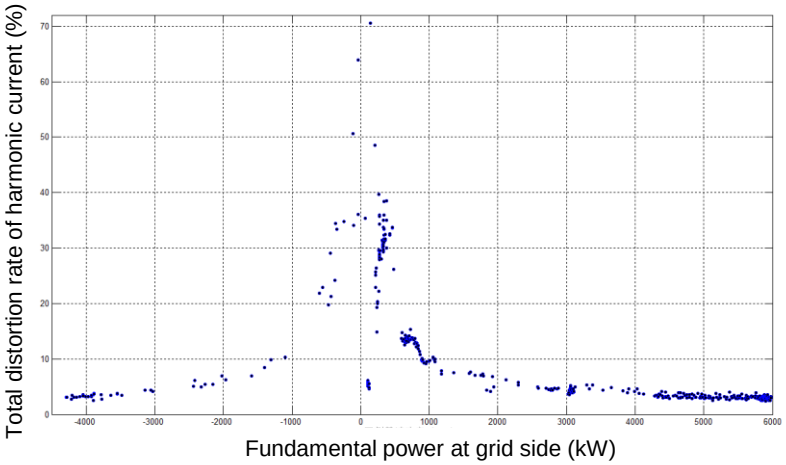

Figure 8 Scatter diagram of correlation between grid side power and total distortion rate of harmonic current

The corresponding distribution characteristics of the total distortion rate of grid side current and grid side power under different powers are shown in Figure 8. The distribution characteristics of total distortion rate of harmonic current are symmetrically distributed along the Y-axis. That is, as long as the power at the grid side is the same, the variation trend of total distortion rate of harmonic current remains the same under both traction and braking conditions.

ISSN: 2710-XXXX DOI: 10.XXXX/jstit.202009_1(1).0001

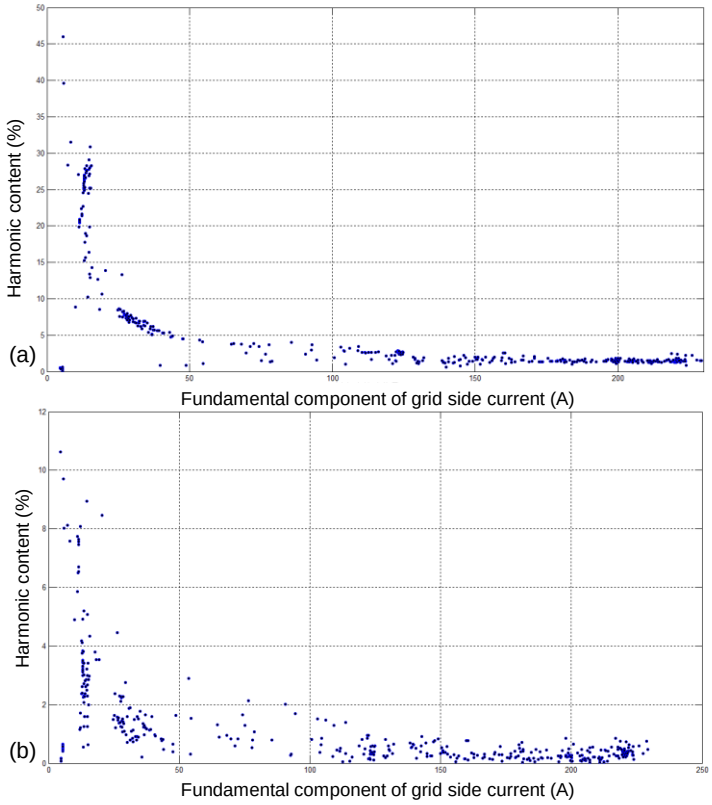

Figure 9 Scatter diagram of correlation between low order harmonic current content and fundamental wave component at grid side, (a) third harmonic, (b) 7th harmonic.

As shown in Figure 9, no matter the 3rd harmonic or 7th harmonic, the harmonic content decreases nonlinearly with the increase of the fundamental component of the grid side current. When the fundamental component is very small, the harmonic content is very large, indicating that the current distortion rate is very high.

ISSN: 2710-XXXX DOI: 10.XXXX/jstit.202009_1(1).0001

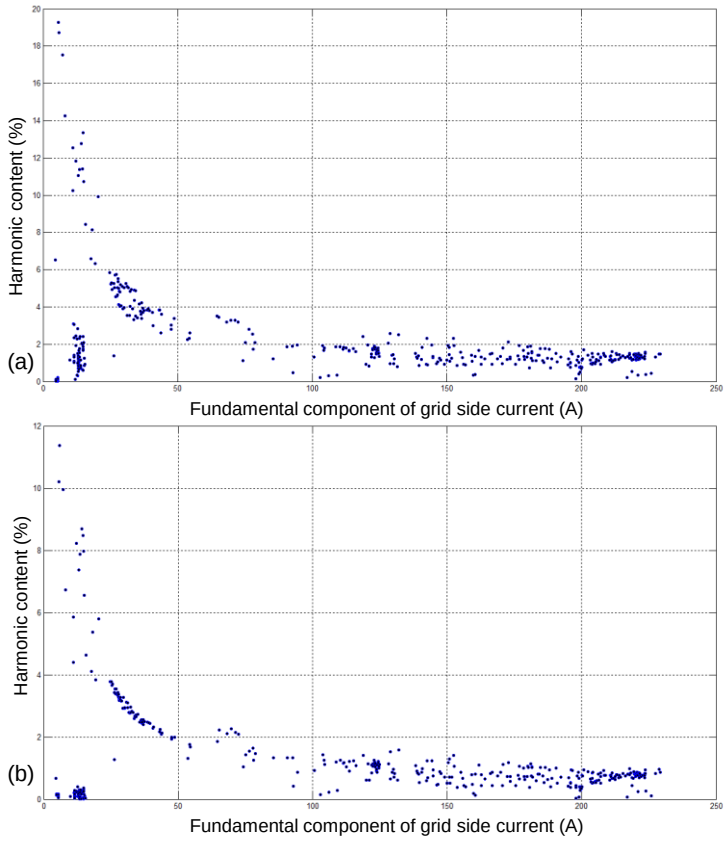

Figure 10 Scatter diagram of correlation between high order harmonic current content and fundamental wave component at grid side, (a) 45th harmonic, (b) 49th harmonic.

It can be seen from the scatter diagram of Figure 10 that the harmonic current is affected by random factors and has a certain randomness. When the fundamental current is small, the total distortion rate of harmonic current is large and the content of single harmonic current is high. When the fundamental current increases, the total distortion rate of harmonic current and the content of single harmonic current decrease significantly.

4 Conclusions

The locomotive simulation model is established and compared with the measured data to study the harmonic characteristics of AC-DC-AC locomotive. Simulation and measured results show that the distribution law of main harmonic times of harmonic current at locomotive grid side is consistent, that is, the characteristic harmonics are mainly distributed in low-order harmonic frequency bands such as 3, 5, 7 and 9 and high-order harmonic frequency bands such as 43, 45, 47, 49, 51 and 53. The harmonic current distribution characteristics of AC-DC-AC locomotive have remarkable correlation with the effective value of fundamental current, showing significant nonlinear attenuation change. That is, when the fundamental current is small, the total distortion rate of harmonic current is large and the content of single harmonic current is high. When the fundamental current increases, the total distortion rate of harmonic current and the content of single harmonic current decrease significantly. At the same time, the harmonic current of locomotive is also affected by random factors, which has certain randomness.

ISSN: 2710-XXXX DOI: 10.XXXX/jstit.202009_1(1).0001

Acknowledgements

The author would like to acknowledge Southwest Jiaotong University Graduate Scholarship, and also thank the support from supervisor.

References

1. Hsiao C. H., *A Haar wavelets method of solving differential equations characterizing the dynamics of a current collection system for an electric locomotive.* Applied Mathematics and Computation, 2015. **265**: 928-935.
2. Liu C., Song Y. M., Bai H., Ma R., Guo X. Z., and Gao F., *Parallel implementation of the auxiliary power system model of the electric locomotive for hardware-in-the-loop simulation.* Iet Power Electronics, 2019. **12**(13): 3521-3526.
3. Liu S., Tian Y., Daniel W. J. T., and Meehan P. A., *Dynamic response of a locomotive with AC electric drives to changes in friction conditions.* Proceedings of the Institution of Mechanical Engineers Part F-Journal of Rail and Rapid Transit, 2017. **231**(1): 90-103.
4. Macian V., Guardiola C., Pla B., and Reig A., *Application and benchmarking of a direct method to optimize the fuel consumption of a diesel electric locomotive.* Proceedings of the Institution of Mechanical Engineers Part F-Journal of Rail and Rapid Transit, 2018. **232**(9): 2272-2289.
5. Saadat M., Esfahanian M., and Saket M. H., *Longitudinal dynamics and energy flow modelling for diesel-electric locomotives.* International Journal of Heavy Vehicle Systems, 2016. **23**(2): 155-170.
6. Saadat M., Esfahanian M., and Saket M. H., *Reducing fuel consumption of diesel-electric locomotives using hybrid powertrain and fuzzy look-ahead control.* Proceedings of the Institution of Mechanical Engineers Part F-Journal of Rail and Rapid Transit, 2017. **231**(4): 406-418.
7. Shao H. D., Jiang H. K., Zhang H. Z., and Liang T. C., *Electric Locomotive Bearing Fault Diagnosis Using a Novel Convolutional Deep Belief Network.* Ieee Transactions on Industrial Electronics, 2018. **65**(3): 2727-2736.
8. Shao H. D., Jiang H. K., Zhao K., Wei D. D., and Li X. Q., *A novel tracking deep wavelet auto-encoder method for intelligent fault diagnosis of electric locomotive bearings.* Mechanical Systems and Signal Processing, 2018. **110**: 193-209.
9. Sharma S. K. and Kumar A., *Impact of electric locomotive traction of the passenger vehicle Ride quality in longitudinal train dynamics in the context of Indian railways.* Mechanics & Industry, 2017. **18**(2).
10. Tao G. Q., Wang L. F., Wen Z. F., Guan Q. H., and Jin X. S., *Measurement and assessment of out-of-round electric locomotive wheels.* Proceedings of the Institution of Mechanical Engineers Part F-Journal of Rail and Rapid Transit, 2018. **232**(1): 275-287.
11. Tao G. Q., Wang L. F., Wen Z. F., Guan Q. H., and Jin X. S., *Experimental investigation into the mechanism of the polygonal wear of electric locomotive wheels.* Vehicle System Dynamics, 2018. **56**(6): 883-899.

ISSN: 2710-XXXX **DOI: 10.XXXX/jstit.202009_1(1).0001**

12. Veselov G. E., Popov A. N., and Radionov I. A., *Synergetic control of asynchronous electric traction drives of locomotives.* Journal of Computer and Systems Sciences International, 2014. **53**(4): 587-600.
13. Yan J. D., Wang H., Huang S. D., and Lan Y. H., *Load Disturbance Observer-Based Complementary Sliding Mode Control for PMSM of the Mine Traction Electric Locomotive.* International Journal of Fuzzy Systems, 2019. **21**(4): 1051-1058.
14. Yasuoka I., Mochizuki Y., Toda S., Nakazawa Y., Gao H. G., and Liu H. Y., *Consideration of Wheel Slip and Readhesion Control for Induction Traction Motor Electric Locomotives with Individual Traction Control.* Electrical Engineering in Japan, 2009. **169**(3): 56-64.
15. Zhang Z. C., Li G., Chu G. F., and Zu H. L., *Dynamic performance analysis of heavy-haul locomotives running through turnout branches with electric brake.* Vehicle System Dynamics, 2020. **58**(7): 1057-1075.
16. Zhao K. H., Li P., Zhang C. F., He J., Li X. F., and Liu J. H., *Optimal Utilization of Adhesion Force for Heavy-Haul Electric Locomotive Based on Extremum Seeking with Sliding Mode and Asymmetric Barrier Lyapunov Function.* Journal of Advanced Transportation, 2019. **2019**.
17. Zhao K. H., Li P., Zhang C. F., He J., Li Y. F., and Yin T. H., *Online Accurate Estimation of the Wheel-Rail Adhesion Coefficient and Optimal Adhesion Antiskid Control of Heavy-Haul Electric Locomotives Based on Asymmetric Barrier Lyapunov Function.* Journal of Sensors, 2018. **2018**.
18. An ThiHoai Thu Anh and Vu Hoang Phuong, *Braking energy recuperation for electric traction drive in urban rail transit network based on control super-capacitor energy storage system.* Journal of Electrical Systems, 2018. **14**(3): 99-114.
19. Chen Zhiwen, Li Xueming, Yang Chao, Peng Tao, Yang Chunhua, Karimi H. R., *A data-driven ground fault detection and isolation method for main circuit in railway electrical traction system.* Isa Transactions, 2019. **87**: 264-271.
20. Fukui Rui, Okabe Taira, Nakao Masayuki, and Honda Yukihiro, *Highly efficient traction drive system with a normal force controller using a piezoelectric actuator.* Advances in Mechanical Engineering, 2017. **9**(10).